


Low-Temperature Properties of Whispering-Gallery Modes in Isotopically Pure Silicon-28

J. Bourhill,^{1,*} M. Goryachev,¹ D.L. Creedon,² B.C. Johnson,³ D.N. Jamieson,³ and M.E. Tobar¹

¹*ARC Centre of Excellence for Engineered Quantum Systems, University of Western Australia, 35 Stirling Highway, Crawley, Western Australia 6009, Australia*

²*School of Physics, University of Melbourne, Victoria 3010, Australia*

³*Centre for Quantum Computation and Communication Technology, School of Physics, University of Melbourne, Parkville, Victoria 3010, Australia*

 (Received 1 November 2018; revised manuscript received 20 February 2019; published 15 April 2019)

Whispering-gallery-(WG) mode resonators are machined from a boule of single-crystal isotopically pure silicon-28. Before machining, the as-grown rod is measured in a cavity, with the best Bragg confined modes exhibiting microwave Q factors on the order of a million for frequencies between 10 and 15 GHz. After machining the rod into smaller cylindrical WG-mode resonators, the frequencies of the fundamental mode families are used to determine the relative permittivity of the material to be 11.488 ± 0.024 near 4 K, with the precision limited only by the dimensional accuracy of the resonator. However, the machining degraded the Q factors to below 4×10^4 . Raman spectroscopy is used to optimize postmachining surface treatments to restore high- Q -factors. This is an enabling step for the use of such resonators for hybrid quantum systems and frequency-conversion applications, as silicon-28 also has very low phonon losses, can host very narrow linewidth spin ensembles, and is a material commonly used in optical applications.

DOI: [10.1103/PhysRevApplied.11.044044](https://doi.org/10.1103/PhysRevApplied.11.044044)

I. INTRODUCTION

In this work we describe investigations of the microwave properties of isotopically purified silicon-28 (^{28}Si). The dielectric properties of the material are close to that of naturally occurring silicon, which is the primary material used in the manufacturing of semiconductor devices. Standard silicon is a mixture of silicon atoms consisting of 28, 29, and 30 nucleons with approximately 92.2%, 4.7%, and 3.1% abundance in nature, respectively. Of these isotopes, only ^{28}Si and ^{30}Si have zero nuclear spin. This feature means that pure crystals of these isotopes act as a so-called “semiconductor vacuum” with respect to a bath of magnetic two-level systems (TLS), leaving the medium inert [1], which is not true for natural silicon. Thus, the absence of nuclear spin in the lattice circumvents one of the most important channels of decoherence, leaving only phonon dissipation, which can be greatly reduced through cooling.

As a result of the lack of nuclear spin, enriched ^{28}Si (i.e., natural silicon depleted in ^{29}Si) has been demonstrated to be an ideal host material for solid-state qubits. Electron or nuclear spins of low-concentration impurities in bulk ^{28}Si can form extremely well-isolated quantum systems. These systems have been shown to exhibit coherence times (T_2)

of up to seconds for the electron spin [2], and minutes for the nuclear spin [3], which are comparable to those of qubits based on trapped ions [4,5]. In addition, isotopically purified silicon has the potential to allow the development of a solid-state clock formed from an ensemble of impurity donors [6], a scheme that has also been proposed for other solid-state mediums [7–9].

The measurement of clock transitions may make use of a microwave-resonant cavity in order to enhance the frequency stability and interaction strengths (and hence coherence times). A common microwave-resonator configuration involves a metal cavity loaded with a cylindrical or spherical dielectric sample in which whispering-gallery (WG) modes [10–14] are excited. These resonant modes are the result of total internal reflection of microwave photons around the air and dielectric boundary at the outer circumference of the crystal. At specific eigenfrequencies dictated by the boundary conditions of the system, electromagnetic resonances may occur with very high confinement of the microwave energy inside the resonator. High azimuthal-order modes have been shown to exhibit quality factors in excess of 2×10^9 [15] at 4 K and 2×10^5 at room temperature [16,17] when excited in low-loss materials such as sapphire, and have thus formed the frequency-determining element for low-phase-noise oscillators. If a silicon crystal could be fabricated in a cylindrical geometry, it could itself act as a low-loss microwave WG-mode

*jeremy.bourhill@uwa.edu.au

resonator. Furthermore, by manufacturing these resonators from enriched silicon, dephasing as a result of nuclear spin interaction could be removed.

Previously, a very low-loss paramagnetic spin ensemble was detected in enriched silicon with a narrow linewidth of less than 7 kHz for a 10 parts per trillion concentration of impurity ions [18]. This was only possible by virtue of the low dielectric photonic losses combined with the long lifetime of the spin transition (low magnetic loss), which enhanced the ac magnetic susceptibility. These results indicate that single crystal ^{28}Si has immense potential for future cavity QED experiments and presents as an excellent candidate for a solid-state clock if impurities that exhibit clock transitions could be purposefully doped within the crystal.

In this work, we present an analysis of WG-mode measurements in an enriched silicon resonator. We characterize the modes and their losses, and discuss the manufacturing and treatment techniques that have been used to improve them.

II. PREPARATION OF ISOTOPICALLY PURE WHISPERING-GALLERY-MODE RESONATORS

A crystal boule approximately 15 mm diameter and 55 mm length is grown using the float zone melting method in an argon atmosphere [19] at the G.G. Devyatikh Institute of Chemistry of High-Purity Substances. The specified concentration of ^{28}Si is 99.993%, with concentration of oxygen and carbon estimated to be less than $1.1 \times 10^{16} \text{ cm}^{-3}$ (on the order of 1 ppm) and boron and phosphorous to be less than $1.1 \times 10^{13} \text{ cm}^{-3}$ (on the order of 1 ppb). The boule as drawn from the melt is cylindrical, with a radius that can clearly be seen to vary by visual inspection. Thus, initial predictions of mode frequencies in the boule are imprecise, making it difficult to properly characterize any photon-spin interactions. To solve this problem, the boule is machined to make four smaller, more

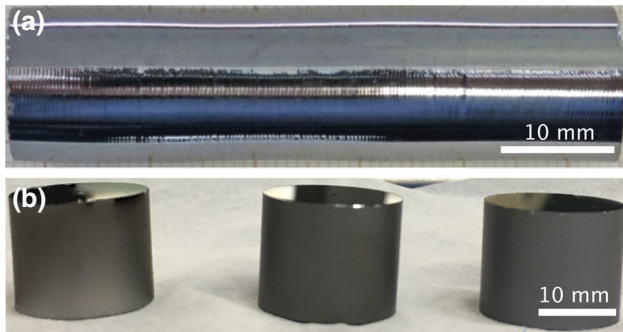


FIG. 1. (a) Photograph of the ^{28}Si rod of 55 mm in length and approximately 15 mm diameter before machining. (b) Three of the four WG-mode ^{28}Si cylindrical resonators cut and machined from the rod.

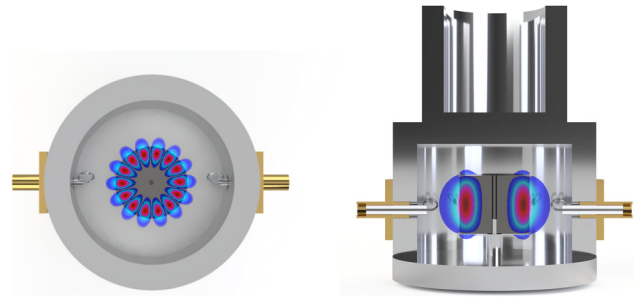


FIG. 2. Graphical representation of the ^{28}Si WG-mode resonator-loaded cavity. The magnitude of the real part of the axial electric field component $|E_z|$ of the 19.535 GHz $\text{WGH}_{7,1,1}$ mode, calculated by finite-element analysis using COMSOL, is shown overlaid on the resonator. (Left) Cross section through in the $r-\theta$ plane at $z = 0$. (Right) Cross section through the $r-z$ plane. The coaxial coupling probes used for excitation and measurement are shown, which couple to the evanescent field of the resonator.

dimensionally precise cylindrical resonators. The crystal is turned to have a uniform cylindrical diameter, which is measured to be 14.455 ± 0.010 mm. This rod is then diced into four equal cylinders of 14.90 mm height, which are optically polished on the end faces and drilled through the axial center of the crystal to a diameter of 1 mm. A photo of the as-grown rod along with three of the diced cylindrical resonators is shown in Fig. 1. Two cavities to house the WG-mode resonators for characterization are then machined from oxygen-free copper and aluminium, each with an integrated support post. A schematic of the resonator-loaded cavity is shown in Fig. 2.

III. CHARACTERIZATION OF ISOTOPICALLY PURE WHISPERING-GALLERY-MODE RESONATORS

The cylindrical WG-mode resonators support quasitransverse electric (WGE) and quasitransverse magnetic (WGH) modes. To allow accurate prediction of these mode frequencies, precise measurements of all dimensions of the cavity and resonator are first made at room temperature. We then calculate the dimensional change at cryogenic temperatures using published values for the coefficient of thermal expansion for all materials. The resulting dimensions are used to define a model in finite-element-analysis software (COMSOL Multiphysics), in which we implement an ultrafine mesh that reduces frequency errors to below that of the dimensional errors of the WG-mode cavity. An example of the computed \vec{E}_z -field density for the $\text{WGH}_{7,1,1}$ mode at 19.535 GHz is shown in Fig. 2, overlaid on top of a 3D rendering of the crystal and housing. Initial simulations are performed using the low-temperature permittivity value for standard float-zone silicon at microwave frequencies published previously [20]. That value, $\epsilon_r = 11.450 \pm$

TABLE I. Calculated and measured mode frequencies of the four modes used to calculate the permittivity.

Mode	Calculated f (GHz)	Measured f (GHz)
WGH _{7,1,1}	19.5353 ± 0.0195	19.5350
WGE _{6,1,1}	19.4163 ± 0.0194	19.4160
WGH _{6,1,1}	17.3010 ± 0.0173	17.3010
WGE _{5,1,1}	17.1831 ± 0.0172	17.1840

0.012, is calculated from the frequencies of higher-order TE_{0,x} modes.

For measurement, the resonator-loaded cavity is placed under vacuum and cooled to as low as 20 mK with a dilution refrigerator. The experimental setup is similar to that used previously for investigations of other materials at low temperature [21–23]. In this setup, the incident microwave signal is attenuated to the level of a few photons by a chain of room temperature and cold attenuators, and the output signal is amplified by a series of cold HEMT and room-temperature amplifiers. These signals are coupled to the resonator using diagonal loop probes to permit coupling to both transverse and axial \vec{H} fields, and hence to both WGH and WGE families.

To further refine the model, a large number of resonant modes are measured with a vector network analyzer (VNA), and identified by comparison with the frequencies calculated in COMSOL. The highest Q -factor modes are exhibited by the fundamental WG-mode families, which allowed easy identification. The frequency and Q factors of the candidate modes are discussed further below. The frequency discrepancy between measured and calculated values allows us to determine more precisely the permittivity of our sample. For WG modes, most of the field is confined within the dielectric crystal, which greatly suppresses perturbations due to the metal support post and cavity walls. Correspondingly, the whispering-gallery-mode technique has been shown previously to be the most

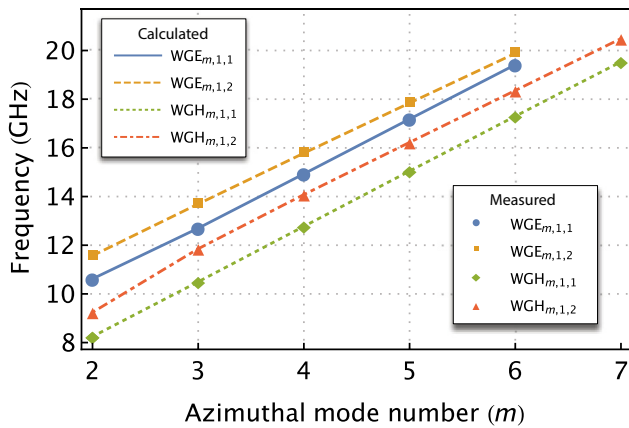


FIG. 3. Measured and calculated mode frequencies of the fundamental WGH and WGE mode frequencies with $\epsilon_r = 11.488$.

accurate for characterizing low-loss crystals [14]. By comparing the four highest frequency WGE_{*m*,1,1} and WGH_{*m*,1,1} modes (as shown in Table I) we determine the permittivity to be $\epsilon_r = 11.4879 \pm 0.0008$. This is the mean value of permittivity, which results in a perfect match between simulation and experiment for the four modes, with the error defined as twice the standard error. This shows excellent relative precision, however, our precision in the dimensions of the cavity are actually much worse, and taking this into account results in a value of $\epsilon_r = 11.488 \pm 0.024$. Using this value, experiment and simulation are compared in Table I and displayed graphically in Fig. 3.

IV. CHARACTERIZATION AND REPAIR OF SURFACE STRAIN

The process of machining the resonators into uniform cylinders resulted in a significant degradation of the microwave Q factors achievable in the sample. To investigate the effect of damage introduced by the lathe turning process, the surfaces of the samples are analyzed

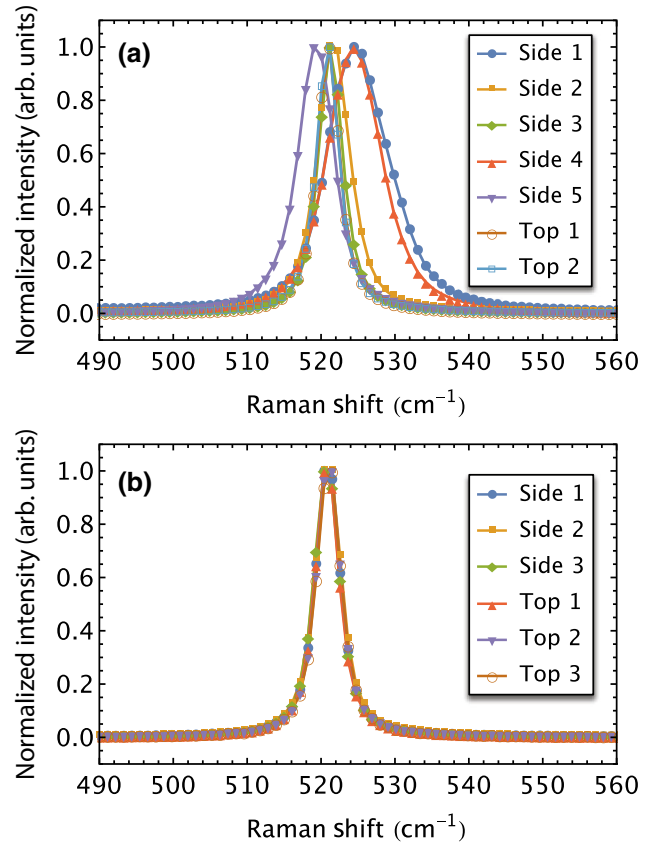


FIG. 4. Raman spectra showing the first-order peak of silicon at 520 cm⁻¹ for one of the WG-mode resonators pictured in Fig. 1. (a) Spectra measured at several locations on the side and top surfaces of the resonator after machining, and (b) after undergoing the acid treatment and annealing procedure. Surface strain is evident in the linewidth broadening and shifting of the Raman peak.

using Raman spectroscopy with results shown in Fig. 4. Raman spectra are acquired by focusing the 532-nm line of a frequency-doubled Nd:YAG laser onto the surface of the resonator with a confocal microscope. A 100× objective lens with a numerical aperture of 0.9 resulting in an approximately 1-μm laser spot size is used, with the laser power set to 15 mW (as measured before the objective) for all measurements. Spectra are collected for 10 s with a Renishaw InVia Reflex 0.25 working distance micro-Raman spectrometer with a 2400 grooves/mm grating. The overall wave-number error is estimated to be ±0.5 cm⁻¹. The spectral resolution of the setup is 1.1 cm⁻¹ per CCD pixel for the 2400 mm⁻¹ grating.

Crystalline silicon has a characteristic Raman peak at 520 cm⁻¹ corresponding to inelastic scattering from the triply degenerate first-order optical phonon modes of silicon (one longitudinal and two transverse optic phonons). Strain or crystal imperfections can introduce linewidth broadening or shifting of this Raman peak. Upon examination, the end faces, which are optically polished showed no such signs of surface strain, with the spectra in several locations nominally identical to that of a calibration sample of (natural abundance) silicon. However, the cylindrical side faces of the resonator exhibited strong variation in the Raman spectrum at several locations, indicating localized strain damage [Fig. 4(a)]. This type of surface damage is known to introduce microwave losses [24,25], and is a likely cause of the low-*Q*-factor values shown in gray in Fig. 5.

To repair the surface damage introduced by machining, standard cleaning and acid-etching steps [26,27] common

in the silicon semiconductor processing industry are first carried out, followed by a high-temperature annealing procedure. The ²⁸Si resonator is first cleaned by sonication in acetone, isopropyl alcohol, and deionized water for 10 min each. This is followed by 10 min clean in Piranha solution [H₂SO₄(70%) and H₂O₂(30%) in a 4:1 ratio] and RCA solution [H₂O, H₂O₂(30%), and HCl(30%) in a 5:1:1 ratio] for 10 min. The resonator is then submerged in a 5% solution of hydrofluoric acid in deionized water for 20 s, and rinsed with deionized water.

An anneal is then performed to relieve surface strain and damage, but additionally to reduce the density of paramagnetic centers on the silicon surface, which may lead to increased microwave losses. This is achieved by annealing in oxygen for 1 h at 1000 °C, followed by a 1 h anneal in nitrogen to ensure a low fixed oxide charge density in the surface oxide. A forming gas anneal (5% H in Ar) at 450 °C for 30 min is then used to passivate dangling bonds at the Si/SiO₂ interface. The density of states at the surface is estimated to be in the low 10¹⁰ cm⁻²/eV for the Si(100)-SiO₂ interface as determined with electrical measurements of a test sample.

After undergoing these treatments, Raman spectra taken at several locations on the crystal indicated repair of surface strain, with no broadening or shifting of the characteristic Raman peak observed [Fig. 4(b)]. The background-corrected Raman data are well modelled using a Voigt function. Fits to the spectra from the as-machined surface have a mean Raman shift of 522.35 cm⁻¹ (standard deviation $\sigma = 2.37$ cm⁻¹), with a mean FWHM linewidth of 11.71 cm⁻¹ ($\sigma = 6.21$ cm⁻¹), compared to a mean

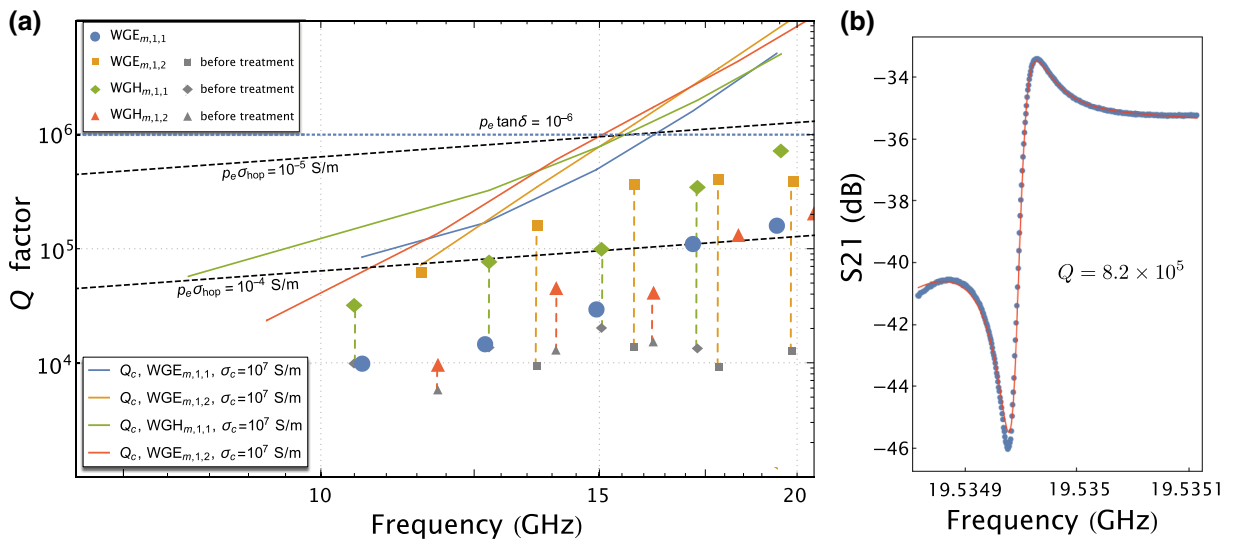


FIG. 5. (a) Measured *Q* factors of the resonator before (gray) and after (coloured) treatment, ensuring enough incident power to obtain maximum *Q* factor. Additionally, potential *Q* factors assuming dominant limiting loss factors are plotted for cavity losses; *Q_c*, assuming a cavity wall conductivity of $\sigma_c = 10^7$ S/m, hopping conductivity; plotted for $p_e \sigma_{hop} = 10^{-5}$ S/m, as well as pure dielectric loss assuming a loss tangent filling factor product $p_e \tan \delta = 10^{-6}$. (b) Transmission spectrum of the WGH_{7,1,1} mode; the highest *Q*-factor mode measured.

Raman shift of 520.95 cm^{-1} ($\sigma = 0.06 \text{ cm}^{-1}$) and FWHM 2.93 cm^{-1} ($\sigma = 0.06 \text{ cm}^{-1}$) for the top surfaces. Such a shift is equivalent to a uniaxial strain of over 0.5 GPa [28]. After the acid treatment and annealing, the Raman data shows good recovery of the crystal, with mean Raman shift 520.9 cm^{-1} ($\sigma = 0.1 \text{ cm}^{-1}$), and FWHM 3.92 cm^{-1} ($\sigma = 0.14 \text{ cm}^{-1}$).

V. MEASUREMENT AFTER SURFACE REPAIR

After processing to relieve surface strain and passivate dangling bonds, the ^{28}Si resonator is placed in an aluminium cavity for cryogenic measurement. Aluminium becomes superconducting below 1.2 K, and thus is used in order to reduce microwave losses in the cavity walls when cooled to millikelvin temperature. In this way, the intrinsic Q factor of the crystal can be determined with the highest accuracy, with minimal influence from other sources of loss such as resistive dissipation in the cavity walls. The measured Q factors before (gray points) and after treatment (coloured points) are plotted in Fig. 5.

The results show that the Q factors after treatment have been restored close to the high values prior to machining [18]. The results indicate that the maximum Q factor is not fully reached given the data in Fig. 5 appears as though Q factors would continue increasing for higher frequency modes.

In order to make predictions on methods to improve Q factors in the future, it is a worthwhile exercise to analyse the potential loss mechanisms in the system and their frequency dependence. Mechanisms considered are losses in the metallic cavity walls, conductivity of the silicon, and dielectric loss. The total Q factor of a resonance can be expressed as

$$\frac{1}{Q} = \sum \frac{1}{Q_i}, \quad (1)$$

where $1/Q_i$ are the losses due to the various mechanisms i , and therefore that which imposes the lowest Q factor determines the final value.

Losses in the metallic cavity walls can be estimated from the geometric factor of each mode, G , where $Q_c^{-1} = R_s/G$. Here R_s is the surface resistivity of the cavity walls at a given frequency and

$$G = \omega \frac{\iiint_V \mu_0 |\mathbf{H}|^2 dv}{\iint_S |\mathbf{H}_\tau|^2 ds}, \quad (2)$$

where S is the internal surface of the cavity, V is the total cavity volume including the silicon sample, and \mathbf{H}_τ is the component of magnetic field tangential to S . As the frequency of modes increases, losses from cavity walls reduce drastically given the explicit frequency dependence of Eq.

(2) and the higher level of energy confinement to the crystal volume for higher-order WG modes, which increases the value of the fraction in Eq. (2).

An alternative loss mechanism is hopping conductivity. At low temperatures, once electrons have been frozen out of the conduction band in a semiconductor, a small amount of conductivity can remain due to electrons associated with impurities, referred to as hopping conductivity, σ_{hop} [20]. These impurities are in very low concentrations and are unevenly distributed throughout the crystal, but the tail ends of their wave functions can overlap, and allow an electron to jump – or “hop” – from one location to another, resulting in conductivity and hence microwave losses [29]. The frequency dependence of conduction losses in general is

$$\frac{1}{Q_{\text{cond}}} = p_e \frac{\sigma}{\omega \epsilon_0 \epsilon_r}, \quad (3)$$

where σ is the conductivity of the resonator, and p_e the electrical filling factor; a measure of the proportion of total electric field contained within the resonator [20]. This loss mechanism has a weaker positive dependence on frequency compared to cavity-wall losses.

An alternative loss mechanism is pure dielectric loss from electronic and ionic polarization, which is frequency independent, assuming constant filling factor, which is approximately 1 for higher-order modes.

From the measured frequency dependence of losses of the modes as shown in Fig. 5, a few conclusions can be made concerning dominant loss mechanisms. The rate at which the Q factor increases as a function of frequency is too large to be attributed to hopping conductivity, however, it is possible this is the limiting loss factor at larger frequencies. The maximum permitted Q factor of hopping conductivity losses is plotted in Fig. 5 with a value of $p_e \sigma_{\text{hop}} = 10^{-5} \text{ S/m}$. This value is chosen so as to permit the largest Q factor measured at 19.535 GHz. This conductivity value would correspond to impurity concentrations less than $4 \times 10^{13} \text{ cm}^{-3}$ [30], which agrees with the quoted concentration from the manufacturer.

Given dielectric loss is approximately frequency independent, the observed frequency dependence can only be explained by metallic cavity-wall losses, which are also plotted in Fig. 5. The values of Q_c are calculated from Eq. (2) assuming surface conductivity of $\sigma_c = 10^7 \text{ S/m}$. This is an order of magnitude assumption chosen to approximate the measured data, and agrees within an order of magnitude of previously measured values [31]. We observe that cavity-wall losses approximate the strong frequency dependence of measured Q factors most closely. At larger frequencies however, the Q factors do not rise sufficiently rapidly to be solely attributed to this mechanism, so the

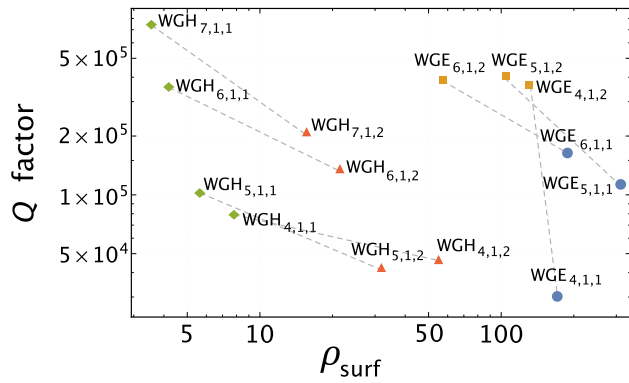


FIG. 6. Measured Q factors categorized into mode families, plotted proportion of normal E field of the curved surface of the cylinder as defined by Eq. (4). The apparent inverse relationship explains the consistent hierarchy of Q factors for each mode family.

system is likely becoming limited by either hopping conductivity or dielectric losses. Measurement of higher frequency modes using a VNA with a higher upper limit of operating frequency should be conducted in the near future to determine if Q factors level out and are therefore limited by dielectric loss or if they continue rising as predicted by hopping conductivity.

One can not rule out that losses in this temperature range may also be attributed to nonuniform dopant distributions in the sample, or the accumulation of charge carriers on the surface of the sample [20]; mechanisms that are more difficult to model. In regards to the latter, a basic calculation of the proportion of electric field normal to the cylindrical surface of the sample at this boundary, formally calculated as

$$\rho_{\text{surf}} = \frac{\iint_S \varepsilon |E_r|^2 ds}{\iiint_V \varepsilon |\mathbf{E}|^2 dV}, \quad (4)$$

suggests that the observed hierarchy of mode Q factors, specifically $Q_{\text{WGE}_{m,1,2}} > Q_{\text{WGE}_{m,1,1}}$ and $Q_{\text{WGH}_{m,1,1}} > Q_{\text{WGH}_{m,1,2}}$, may be attributed to this parameter. That is, the more electric field leaving the crystal surface radially, the larger the losses potentially due to surface charges. Figure 6 shows ρ_{surf} versus Q factor, and indeed we see that at least within the same polarization of mode (E or H), there is a correlation between proportion of surface radial \vec{E} field and Q . Furthermore, it is worth noting that $\text{WGE}_{m,1,1}$ modes are unable to be identified before surface treatment due to their low- Q factors, which may be explained by this family having the largest ρ_{surf} values of all the modes.

In regards to losses arising from some anisotropy in the crystal such as nonuniform conductivity or dopant distribution, one would not expect the orderly relationship observed between Q factor and frequency, and therefore this can likely be ruled out as a limiting mechanism.

VI. CONCLUSION

The construction of WG-mode resonators from isotopically pure silicon is a promising research direction given the enhanced Q factors (and hence coherence time) of such electromagnetic resonances. We successfully demonstrate the construction of these resonators and a technique to recover the high- Q -factors postmachining, which are initially lost due to surface strain imposed on the crystal and revealed through Raman spectroscopy. This result is crucial for the use of such resonators for hybrid quantum systems and frequency-conversion applications, given silicon-28 has very low phonon losses, can host very narrow linewidth spin ensembles, and is a material commonly used in optical applications. The next step will be to purposefully implant impurity ions and heal the implantation damage to recover the silicon lattice. In this way, narrow linewidth spin ensembles with clock transitions may be realized, which will couple to high- Q WG modes inside the crystal.

ACKNOWLEDGMENTS

This work is supported by Australian Research Council Grants No. CE170100009, No. CE170100012, a Research Collaboration Award from the University of Western Australia and the Defence Next Generation Technology Program.

- [1] Gary Wolfowicz, Alexei M. Tyryshkin, Richard E. George, Helge Riemann, Nikolai V. Abrosimov, Peter Becker, Hans-Joachim Pohl, Mike L. W. Thewalt, Stephen A. Lyon, and John J. L. Morton, Atomic clock transitions in silicon-based spin qubits, *Nat. Nanotechnol.* **8**, 881 (2013).
- [2] Alexei M. Tyryshkin, Shinichi Tojo, John J. L. Morton, Helge Riemann, Nikolai V. Abrosimov, Peter Becker, Hans-Joachim Pohl, Thomas Schenkel, Michael L. W. Thewalt, Kohei M. Itoh, and S. A. Lyon, Electron spin coherence exceeding seconds in high-purity silicon, *Nat. Mater.* **11**, 143 (2011).
- [3] M. Steger, Quantum information storage for over 180 s using donor spins in a ^{28}Si ‘semiconductor vacuum’, *Science* **336**, 1280 (2012).
- [4] P. C. Haljan, P. J. Lee, K.-A. Brickman, M. Acton, L. Deslauriers, and C. Monroe, Entanglement of trapped-ion clock states, *Phys. Rev. A* **72**, 062316 (2005).
- [5] C. Langer, R. Ozeri, J. D. Jost, J. Chiaverini, B. DeMarco, A. Ben-Kish, R. B. Blakestad, J. Britton, D. B. Hume, W. M. Itano, D. Leibfried, R. Reichle, T. Rosenband, T. Schaetz, P. O. Schmidt, and D. J. Wineland, Long-Lived Qubit Memory using Atomic Ions, *Phys. Rev. Lett.* **95**, 060502 (2005).
- [6] K. Saeedi, M. Szech, P. Dluhy, J. Z. Salvail, K. J. Morse, H. Riemann, N. V. Abrosimov, N. Nötzel, K. L. Litvinenko, B. N. Murdin, and M. L. W. Thewalt, Optical pumping and readout of bismuth hyperfine states in silicon for atomic clock applications, *Sci. Rep.* **5**, 10493 (2015).

- [7] Liang Jin, Matthias Pfender, Nabeel Aslam, Philipp Neumann, Sen Yang, Jörg Wrachtrup, and Ren-Bao Liu, Proposal for a room-temperature diamond maser, *Nat. Commun.* **6**, 8251 (2015).
- [8] J. S. Hodges, N. Y. Yao, D. Maclaurin, C. Rastogi, M. D. Lukin, and D. Englund, Timekeeping with electron spin states in diamond, *Phys. Rev. A* **87**, 032118 (2013).
- [9] Maxim Goryachev, Stuart Watt, Jeremy Bourhill, Mikhail Kostylev, and Michael E. Tobar, Cavity magnon polaritons with lithium ferrite and three-dimensional microwave resonators at millikelvin temperatures, *Phys. Rev. B* **97**, 155129 (2018).
- [10] M. E. Tobar and A. G. Mann, Resonant frequencies of higher order modes in cylindrical anisotropic dielectric resonators, *IEEE Trans. Microw. Theory. Tech.* **39**, 2077 (1991).
- [11] Michael Edmund Tobar, Jerzy Krupka, Eugene Nicolay Ivanov, and Richard Alex Woode, Anisotropic complex permittivity measurements of mono-crystalline rutile between 10 and 300 K, *J. Appl. Phys.* **83**, 1604 (1998).
- [12] Anatolii N. Oraevsky, Whispering-gallery waves, *Quantum Elec.* **32**, 377 (2002).
- [13] A. B. Matsko, A. A. Savchenkov, D. Strekalov, V. S. Ilchenko, and L. Maleki, Review of applications of whispering-gallery mode resonators in photonics and nonlinear optics, *Interplanetary Network Prog. Rep.* **162**, 1 (2005).
- [14] J. Krupka, K. Derzakowski, A. Abramowicz, M. E. Tobar, and R. G. Geyer, Use of whispering-gallery modes for complex permittivity determinations of ultra-low-loss dielectric materials, *IEEE Trans. Microw. Theory Tech.* **47**, 752 (1999).
- [15] Daniel L. Creedon, Yarema Reshitnyk, Warrick Farr, John M. Martinis, Timothy L. Duty, and Michael E. Tobar, High q-factor sapphire whispering gallery mode microwave resonator at single photon energies and millikelvin temperatures, *Appl. Phys. Lett.* **98**, 222903 (2011).
- [16] M. E. Tobar, E. N. Ivanov, R. A. Woode, J. H. Searls, and A. G. Mann, Low noise 9-GHz sapphire resonator-oscillator with thermoelectric temperature stabilization at 300 Kelvin, *IEEE Microwave Guided Wave Lett.* **5**, 108 (1995).
- [17] E. N. Ivanov and M. E. Tobar, Low phase-noise sapphire crystal microwave oscillators: Current status, *IEEE Trans. Ultrason. Ferroelectr. Freq. Control* **56**, 263 (2009).
- [18] Nikita Kostylev, Maxim Goryachev, Andrey D. Bulanov, Vladimir A. Gavva, and Michael E. Tobar, Determination of low loss in isotopically pure single crystal ^{28}Si at low temperatures and single microwave photon energy, *Sci. Rep.* **7**, 44813 (2017).
- [19] Kohei M. Itoh, Jiro Kato, Masafumi Uemura, Alexey K. Kaliteevskii, Oleg N. Godisov, Grigori G. Devyatych, Andrey D. Bulanov, Anatoli V. Gusev, Igor D. Kovalev, Pyotr G. Sennikov, Hans J. Pohl, Nikolai V. Abrosimov, and Helge Riemann, High purity isotopically enriched ^{29}Si and ^{30}Si single crystals: Isotope separation, purification, and growth, *Jpn. J. Appl. Phys.* **42**, 6248 (2003).
- [20] J. Krupka, J. Breeze, A. Centeno, N. Alford, T. Claussen, and L. Jensen, Measurements of permittivity, dielectric loss tangent, and resistivity of float-zone silicon at microwave frequencies, *IEEE Trans. Microwave Theory Tech.* **54**, 3995 (2006).
- [21] Warrick G. Farr, Daniel L. Creedon, Maxim Goryachev, Karim Benmessai, and Michael E. Tobar, Ultrasensitive microwave spectroscopy of paramagnetic impurities in sapphire crystals at millikelvin temperatures, *Phys. Rev. B* **88**, 224426 (2013).
- [22] Maxim Goryachev, Warrick G. Farr, and Michael E. Tobar, Giant g-factors of natural impurities in synthetic quartz, *Appl. Phys. Lett.* **103**, 262404 (2013).
- [23] Maxim Goryachev, Nikita Kostylev, and Michael E. Tobar, Single-photon level study of microwave properties of lithium niobate at millikelvin temperatures, *Phys. Rev. B* **92**, 060406 (2015).
- [24] R. C. Taber and C. A. Flory, Microwave oscillators incorporating cryogenic sapphire dielectric resonators, *IEEE Trans. Ultrason. Ferroelectr. Freq. Control* **42**, 111 (1995).
- [25] V. B. Braginsky, V. P. Mitrofanov, V. I. Panov, and Robert Krotkov, Systems with small dissipation, *Am. J. Phys.* **55**, 1153 (1987).
- [26] W. Kern and D. A. Puotinen, Cleaning solutions based on hydrogen peroxide for use in silicon semiconductor technology, *RCA Rev.* **31**, 187 (1970).
- [27] Werner Kern, The evolution of silicon wafer cleaning technology, *J. Electrochem. Soc.* **137**, 1887 (1990).
- [28] Ingrid De Wolf, H. E. Maes, and Stephen K. Jones, Stress measurements in silicon devices through raman spectroscopy: Bridging the gap between theory and experiment, *J. Appl. Phys.* **79**, 7148 (1996).
- [29] B. I. Shklovskii and A. L. Efros, *Electronic Properties of Doped Semiconductors* (Springer, Berlin, Heidelberg, 1984).
- [30] E. H. Putley and W. H. Mitchell, The electrical conductivity and Hall effect of silicon, *Proc. Phys. Soc.* **72**, 193 (1958).
- [31] E. Pytte, Contribution of the electron-phonon interaction to the effective mass, superconducting transition temperature, and the resistivity in aluminium, *J. Phys. Chem. Solids* **28**, 93 (1967).